



Bubble Dynamics and Enhanced Heat Transfer During High-Pressure Pool Boiling on Rough Surface

Avdhoot Walunj*

Dr. A. S. College of Agriculture Engineering and Technology, Rahuri 413 722, India
and

A. Sathyabhama†

National Institute of Technology Karnataka, Surathkal 575 025, India

DOI: 10.2514/1.T5495

In the present study, the influence of surface roughness (R_a) on critical heat flux (CHF) of water at pressure of 1, 5, and 10 bar is investigated. The desired value of R_a is achieved by making unidirectional scratches on the flat copper surface. Surface roughness R_a varies from 0.106 to 4.03 μm . The high-speed camera of 1000 fps is used for the boiling visualization study. The effect of surface roughness on bubble departure diameter and bubble frequency at different pressure is reported. Kim's CHF model is modified to include the contact angle as a function of surface roughness and temperature, which predicts the experimental CHF with mean absolute error (MAE) of 10.50% at pressure up to 10 bar. The correlation developed for bubble departure diameter predicts the experimental values with MAE of 17.09%. The relation between bubble departure diameter and bubble frequency is also developed, which predicts the corresponding experimental values with MAE of 25.26%.

Nomenclature

A	=	amplitude of oscillation
Ar	=	Archimedes number
Bo	=	Bond number
C	=	constant
C_d	=	bubble drag coefficient
C_L	=	lift coefficient
C_p	=	specific heat, $\text{J}/(\text{kg} \cdot \text{K})$
C_s	=	empirical constant in force term
C_t	=	the proportionality factor
c_1	=	a parameter
D_b	=	bubble departure diameter, mm
d	=	instantaneous bubble diameter, mm
F	=	force, N
f	=	bubble frequency, s^{-1}
g	=	gravity, m/s^2
h	=	heat transfer coefficient, $\text{W}/(\text{m}^2 \cdot \text{K})$
h_{fg}	=	latent heat, J/kg
Ja	=	Jakob number
Ja^c	=	modified Jakob number
K	=	term in the CHF model
k_{cu}	=	thermal conductivity of copper, $\text{W}/(\text{m} \cdot \text{K})$
N	=	exponent in the correlation
P	=	pressure, bar
Pr	=	Prandtl number
q''	=	heat flux, W/m^2
R_a	=	average roughness, μm
R_q	=	root mean squared roughness, μm
R_z	=	10-point average roughness, μm
r	=	radius, mm
S	=	accommodation factor
S_m	=	mean spacing, μm
T	=	temperature, $^\circ\text{C}$

t_g	=	growth period, ms
t_w	=	waiting period, ms
x	=	distance, mm
ΔT	=	wall superheat, $^\circ\text{C}$
θ	=	contact angle, deg
Φ	=	angle of inclination, deg
μ	=	viscosity, $(\text{N} \cdot \text{s})/\text{m}^2$
ρ	=	density, kg/m^3
σ	=	surface tension, N/m
α	=	thermal diffusivity, m^2/s
ω	=	fitting parameter

Subscripts

bi	=	bubble inertia
buy	=	buoyancy
CHF	=	critical heat flux
duy	=	unsteady growth
g	=	gravity
L	=	lift
l	=	liquid
st	=	surface tension
v	=	vapor
w	=	wall

I. Introduction

Thermal management of high-power-density compact devices in the space application is a challenge [1–3]. Pool boiling is a mode of heat transfer that can efficiently transfer the heat generated in such compact devices. Critical heat flux (CHF) occurs when the liquid layer adjacent to the boiling surface completely evaporates and vapor layer occupies the entire boiling surface. It is a critical parameter in the pool boiling study as the sudden drop in the heat transfer coefficient after CHF may lead to the failure of compact devices. The overheating problems in the compact devices can be resolved by the CHF enhancement. It will also increase the thermal efficiency of the system. Passive techniques of CHF enhancement, which do not require the external power during their operation, are the most suitable for space applications. The CHF enhancement by various types of passive techniques, such as rough surface, nanofluid, structured surface, and surface coating, have been reported in the literature [4–10]. The mechanism of the pool boiling that leads to the CHF should be understood to avoid the thermal breakdown in the space applications. Hydrodynamic instability or macro/microlayer evaporation theory was proposed two decades before and thereafter

Received 13 March 2018; revision received 19 June 2018; accepted for publication 25 July 2018; published online 12 October 2018. Copyright © 2018 by the American Institute of Aeronautics and Astronautics, Inc. All rights reserved. All requests for copying and permission to reprint should be submitted to CCC at www.copyright.com; employ the ISSN 0887-8722 (print) or 1533-6808 (online) to initiate your request. See also AIAA Rights and Permissions www.aiaa.org/randp.

*Assistant Professor, Department of Farm Machinery and Power Engineering; also Research Scholar, Department of Mechanical Engineering, Boiling Heat Transfer Laboratory (Corresponding Author).

†Associate Professor, Department of Mechanical Engineering.

Table 1 Value of K in the correlation given in Eq. (1)

Reference	K
Kutateladze [11]	0.13–0.19
Zuber [12]	0.131
Lienhard and Dhir [13]	0.149
Kandlikar [14]	$\left(\frac{1 + \cos\theta}{16}\right) \left[\frac{2}{\pi} + \frac{\pi}{4}(1 + \cos\theta)\cos\theta\right]^{1/2}$
Kim et al. [15]	$S \left(\frac{1 + \cos\theta}{16}\right) \left[\frac{2}{\pi} + \frac{\pi}{4}(1 + \cos\theta) + \frac{4C\cos\theta}{1 + \cos\theta} \left(\frac{R_a}{S_m}\right)\right]^{1/2}$

modified by many investigators to justify the cause of CHF. Various semi-empirical correlations for CHF are proposed in the form of Eq. (1). The value of K proposed by researchers is given in Table 1.

$$q_{\text{CHF}} = Kh_{fg}\rho_v^{1/2}[\sigma g(\rho_l - \rho_v)]^{1/4} \quad (1)$$

Kutateladze [11] proposed the correlation based on the hydrodynamic consideration that causes the instability in the liquid-vapor flow near the boiling surface. Hydrodynamic instability model was proposed by Zuber [12] considering the Helmholtz instability at liquid-vapor interface that leads to the CHF. Lienhard and Dhir [13] modified Zuber's model for the large and upward facing surface. Kandlikar [14] for the first time developed a model by considering the role of contact angle followed by force balance approach having compatibility with different fluids. The CHF model was developed by the force balance among growth forces, gravity, and surface tension. Moreover, the effect of angle of inclination of the surface on the CHF has also been incorporated in the model, as given in Table 1. Kim et al. [15] modified Kandlikar's model by adding surface roughness (R_a) parameter. They assumed that the single scratch acts as a capillary tube. Therefore, they considered that a number of capillary tubes lie underneath the bubble and thus estimated the capillary force acting on the growing bubble. Along with the CHF prediction, it is vital to study the bubble dynamics to understand the mechanism of pool boiling. Measurement of bubble diameter and bubble frequency also helps to predict the CHF. Bubble departure diameter and bubble frequency are influenced by the unsteady growth force, surface tension force, and buoyancy force. Few well-known correlations for prediction of bubble departure diameter and bubble frequency at high pressure are presented in Table 2. The correlations for bubble departure diameter presented by Cole [16], Cole and Rohsenow [17], and Cole and Shulman [18] are found to be the function of surface temperature, surface tension, and properties of liquid and vapor. The

correlation of Cole and Rohsenow [17] includes the modified Jakob number (Ja^c) as a function of saturation temperature, whereas the correlation of Cole and Shulman [18] considers the inverse relation between bubble departure diameter and system pressure. The correlation for the relationship between bubble departure diameter and bubble departure frequency is found in the form of fD_b^n . Chen et al. [19] recently developed the correlation for fD_b^2 at pressure up to 4 bar, considering the unsteady bubble growth under the influence of various forces. The empirical constant of the correlation is obtained by the best fit of their experimental values.

In the present work, the effect of surface roughness on pool boiling of water at pressure up to 10 bar is studied. The CHF is predicted by considering the effect of temperature and R_a on contact angle. The high-speed visualization is carried to monitor the bubble growth at a different pressure, and thus bubble departure diameter and bubble frequency are measured for various experimental conditions. The influence of R_a on bubble departure diameter and bubble frequency at a different Jakob number (Ja) is studied. The correlation for D_b and fD_b^2 is presented at high-pressure boiling condition of the distilled water.

II. Experimentation

A. Preparation and Characterization of Test Samples

The top surface of six samples is polished by the 2000-grit sandpaper to remove the contamination and to obtain uniform surface finishing. The smooth and flat surface of copper sample is used to form unidirectional scratches by 1200-, 800-, 600-, 120-, 80-, and 60-grit SiC sandpapers. The number of strokes is gradually increased with the increase in grit size of the sandpaper. Uniform pressure and continuous distilled water supply on the polishing surface are maintained during each turn. After polishing, all samples are sequentially cleaned in acetone, ethanol, and distilled water. Thereafter samples are characterized by wettability and roughness measurement. The static contact angle of the 10 μl water droplet for each sample is measured using goniometer (GBX Digidrop). The roughness parameter is measured using roughness tester (Mitutoyo). Each sample is tested at six different locations where unidirectional scratches are perpendicular to the direction of the testing probe. The evaluation length is 4 mm. The uniformity of the roughness values is ensured over the entire surface by permitting $\pm 0.1 \mu\text{m}$ variation in the readings of six different locations.

B. Experimental Setup

The experimental setup, as shown in Fig. 1, mainly includes a boiling chamber, test section, condenser unit, and CCD camera. The rectangular chamber has removable top and bottom flanges. The top flange is integrated with condenser coil, whereas the test section is fitted to bottom flange. K-type thermocouple and pressure transducer are inserted into the boiling chamber to measure the bulk fluid temperature (T_f) and chamber pressure, respectively. Transparent borosilicate glass is provided to the wall of boiling chamber for the visualization study. Auxiliary heaters of 2000 W capacity are used to maintain the saturation condition of the distilled water. The setup is integrated with the NI-9213 temperature module to acquire temperature readings.

Table 2 Correlations for bubble departure diameter and for the relationship between bubble departure diameter and bubble departure frequency

Reference	Correlation
Cole [16]	$D_b = 0.04Ja \left[\frac{\sigma}{g(\rho_l - \rho_v)}\right]^{1/2}$
Cole and Rohsenow [17]	$D_b = c_1 \left[\frac{\sigma}{g(\rho_l - \rho_v)}\right]^{1/2} Ja^c(5/4)$
Cole and Shulman [18]	$D_b = P^{-1} \left[\frac{\sigma}{g(\rho_l - \rho_v)}\right]^{1/2}$
Cole [25]	$fD_b^{1/2} = \left[\frac{4g(\rho_l - \rho_v)}{3Cd\rho_l}\right]^{1/2}$
Zuber [26]	$fD_b = 0.59 \left[\frac{\sigma g(\rho_l - \rho_v)}{\rho_l^2}\right]^{1/4}$
Jakob and Fritz [27]	$fD_b = 0.078$

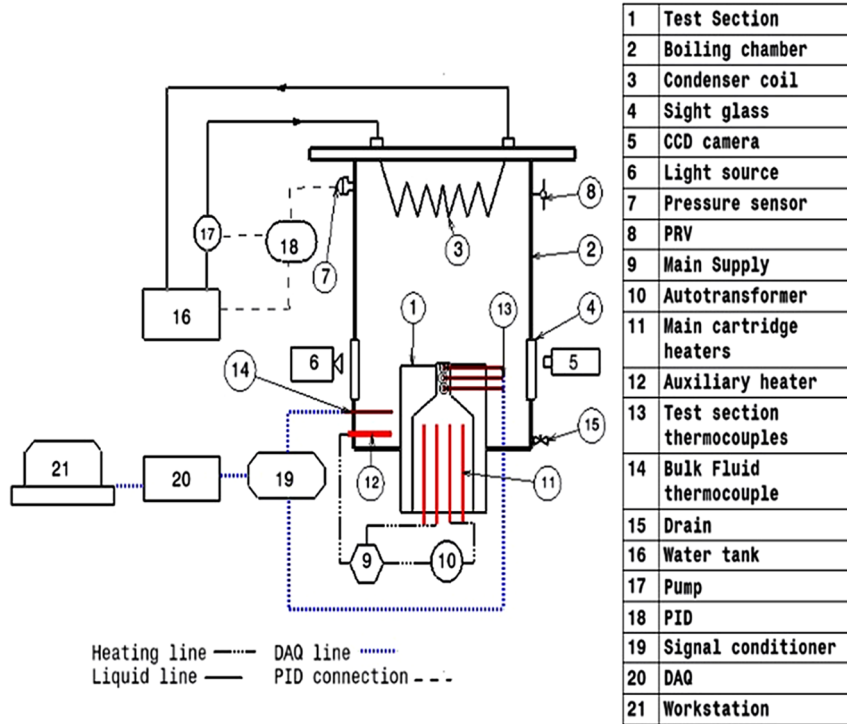
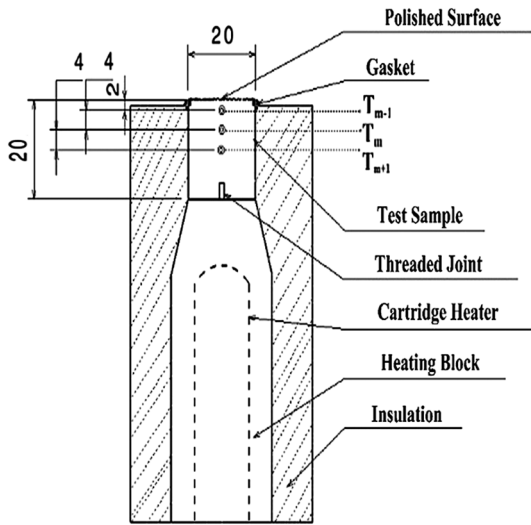


Fig. 1 Experimental setup.



All the dimensions are in mm
Fig. 2 Test section.

C. Test Section

Copper samples of 20 mm diameter and 20 mm length are prepared and characterized. The high-density cartridge heaters are inserted in the heating block. The sample is fixed on the heating block with perfect surface contact. The assembly of sample and heating block is perfectly insulated with glass wool bed as shown in Fig. 2. An O-ring and high-temperature noncorrosive RTV silicone gasket are used between the test sample and insulation block to prevent leakage and to avoid edge effect during the boiling test. K-type sheathed thermocouples of 1 mm diameter are used to measure the temperature of the test sample at different locations. The thermocouples are implanted at 2, 6, and 10 mm in the test sample from the top surface and the temperatures T_{m-1} , T_m , and T_{m+1} correspond to these thermocouple readings, respectively.

D. Experimental Procedure

The characterized sample is sequentially cleaned by acetone, ethanol, and distilled water before each trial. The quantity of water used is fixed for all trials. Before each trial, the pool of water is rigorously boiled to remove the dissolved gases. Experiments are performed by supplying incremental heat through wattmeter. Steady state of the system is recognized after certain time interval, and corresponding temperature is recorded through data acquisition system. The pressure in the chamber is maintained by a proportional integral derivative (PID) pressure controller system.

The main heater and test sample are considered as the axisymmetric system. Because of uniform surface roughness, the heat flux from the surface is considered as uniform. The heat flux dissipated to the boiling fluid and the surface temperature can be estimated by the thermocouple readings.

The heat flux from the top surface of the sample is calculated by Eq. (2).

$$q'' = -k_{Cu} \frac{T_{m-1} - T_{m+1}}{2\Delta x} \quad (2)$$

where Δx is the distance between two thermocouples.

The surface temperature of the sample is calculated by using Eq. (3).

$$T_w = T_{m-1} - q'' \left(\frac{x_{m-1}}{k_{Cu}} \right) \quad (3)$$

where x_{m-1} is the distance between the surface of a sample and a top thermocouple (T_{m-1}) and is equal to 2 mm, as shown in Fig. 2.

Heat transfer coefficient (HTC) between the surface and water is estimated by Eq. (4).

$$h = \frac{q''}{(T_w - T_l)} \quad (4)$$

E. Visualization of Boiling

A high-speed visualization is conducted by AOS Promon 501 camera of 1000 frames/s with resolution of 480×240 pixel. AF NIKKOR 50 mm F/1.4D lens is installed. The camera and diffused light source are kept opposite as shown in Fig. 1. The camera is positioned in-line with the flat surface. The computer is coupled with the camera through Promon software. The software provides interface to video recording and frame conversion. Selected images at the bubble departure are loaded into the MATLAB image-processing tool to measure the horizontal and vertical dimensions of the bubble meniscus in terms of pixels. The mean of both the dimensions is considered as the bubble departure diameter.

F. Uncertainty

The uncertainty calculations are done by the propagation of error method, as discussed in [20]. The uncertainty in temperature and distance measurement is $\pm 0.1^\circ\text{C}$ and ± 0.0001 m, respectively. The uncertainty in pressure measurement is $\pm 0.2\%$ (full span is 0–27.4 bar). At high temperature, the uncertainty in the heat flux is found to be 8.07%, whereas the uncertainty in the surface temperature lies between 0.14 to 0.17°C throughout the experiments. The uncertainty in the HTC is found to be 8.19% at the higher operating temperature. The uncertainty in the measurement of bubble departure diameter is 0.05 mm. The maximum uncertainty in the bubble frequency is estimated to be 10.45%.

III. Results and Discussion

The roughness parameters of each sample obtained during roughness measurement are given in Table 3. The average value of contact angle measured before and after the boiling test for each R_a is plotted in Fig. 3. The relation between contact angle and R_a obtained by the best fitting curve is given in Fig. 3. It is observed that the contact angle decreased at higher surface roughness value ($R_a \geq 3.17 \mu\text{m}$). Each unidirectional scratch acts as a capillary tube. The radius of the capillary tube increases with the increase in R_a . Thus, capillary wicking through the unidirectional scratches becomes dominant for the sample of higher surface roughness. Hence, the surface of higher roughness turns into hydrophilic, which results in the drop in the contact angle.

A. Boiling Curve

Pool boiling experiments are conducted with the copper sample of R_a ranging from 0.103 to $4.03 \mu\text{m}$ at pressure 1, 5, and 10 bar. Representative boiling curves for different values of R_a at $P = 10$ bar are shown in Fig. 4, which clearly shows that the boiling curve shifts toward left with the increase in R_a . This demonstrates the enhanced nucleate boiling heat transfer performance due to the increase in R_a . The onset of boiling temperature is also found to be reduced with the increase in R_a . The variation in HTC of water for different values of R_a with heat flux is shown in Fig. 5 at $P = 10$ bar. The curve shifts upward with the increase in R_a , which justifies the augmentation in HTC due to increase in the R_a .

B. Critical Heat Flux

The various boiling phases are identified during the visualization study that is conducted using a high-speed camera. Table 4 illustrates the boiling phases observed for $R_a = 4.03 \mu\text{m}$ at different pressures.

Table 3 Roughness parameters in μm

R_a	R_z	R_q	S_m
0.106	1.20	0.14	13.2
0.83	7.05	1.07	26.8
1.87	13.30	2.40	35.7
3.17	22.91	4.12	42.2
3.59	27.55	4.09	44.8
4.03	26.50	4.95	45.2

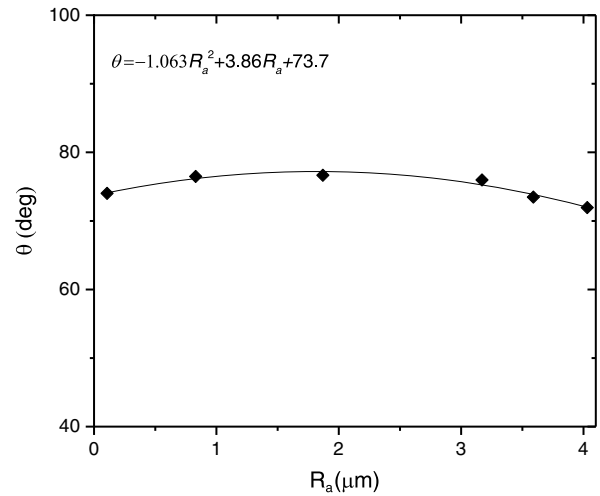


Fig. 3 Variation in static contact angle with R_a .

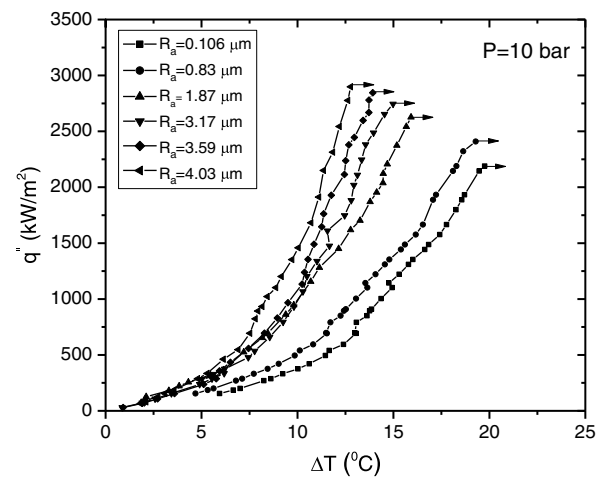


Fig. 4 Boiling curves of the sample of R_a ranging from 0.103 to $4.03 \mu\text{m}$ at 10 bar.

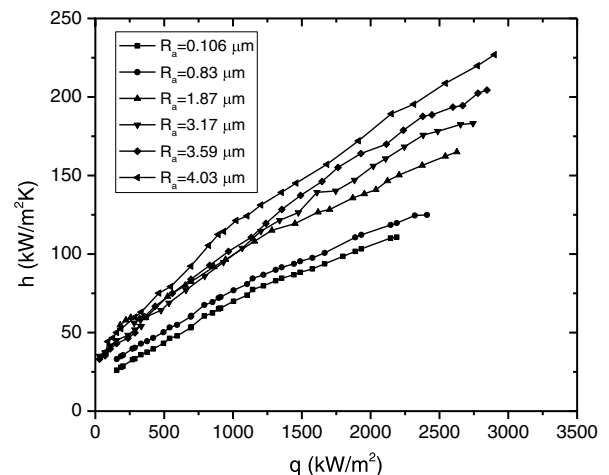
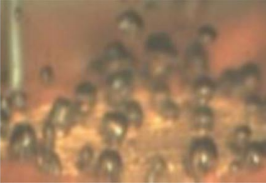


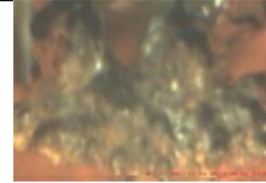
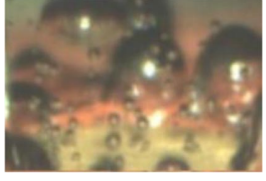
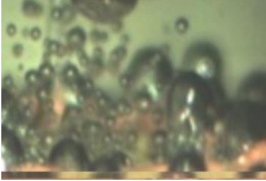



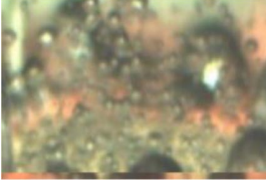

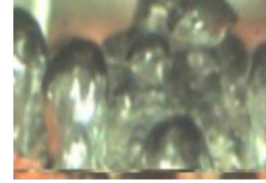


Fig. 5 Variation in HTC with q'' at different R_a at 10 bar.

It is observed that the discrete bubble forms at the onset of boiling and the number of such discrete bubbles increases with the increase in the wall superheat. The moment at which the entire surface is covered by discrete bubbles is termed as “fully developed nucleate boiling phase.” Thereafter, vertical bubble coalescence is observed that forms

Table 4 Boiling phases for $R_a = 4.03 \mu\text{m}$ at different pressures

Pressure	Onset of boiling	Nucleate boiling	Fully developed nucleate boiling	Vapor blanket (CHF)
$P = 1 \text{ bar}$				
	$q'' = 270.82 \text{ kW/m}^2$	$q'' = 553.50 \text{ kW/m}^2$	$q'' = 787.02 \text{ kW/m}^2$	$q'' = 1690.78 \text{ kW/m}^2$
$P = 5 \text{ bar}$				
	$q'' = 257.02 \text{ kW/m}^2$	$q'' = 551.81 \text{ kW/m}^2$	$q'' = 1194.99 \text{ kW/m}^2$	$q'' = 2025.78 \text{ kW/m}^2$
$P = 10 \text{ bar}$				
	$q'' = 287.35 \text{ kW/m}^2$	$q'' = 694.29 \text{ kW/m}^2$	$q'' = 1458.03 \text{ kW/m}^2$	$q'' = 2543.40 \text{ kW/m}^2$

a vapor column over the nucleation site. The horizontal bubble coalescence is retarded due to the capillary action in the unidirectional scratches as shown in Fig. 6. This ensures the continuous liquid supply to the nucleation sites that retard the vapor from spreading over the entire surface. Thus heat flux enhances due to the increase in the R_a .

At high heat flux, bubble spreads horizontally to form vapor blanket over the entire surface. At this moment a large vapor bubble occupies the complete surface. This vapor blanket acts as a barrier for the heat transfer from the surface to the liquid, which results in the reduction of HTC. The phase that has a upper limit of heat transfer is recognized as CHF. The HTC of water at CHF is found to be maximum and thereafter it dropped with the increase in the heat flux. The heat flux corresponding to the upper limit of HTC value for each R_a is identified and CHF is plotted in Fig. 7. It is found that CHF increases with the increase in system pressure. At $P = 1 \text{ bar}$, the CHF of $R_a = 0.106 \mu\text{m}$ is 876.72 kW/m^2 , whereas at $P = 10 \text{ bar}$, CHF of $R_a = 0.106 \mu\text{m}$ is 2189.45 kW/m^2 . The CHF of $R_a = 4.03 \mu\text{m}$ at 1, 5, and 10 bar is found to be 92.85, 47.11, and 32.38% higher than that of $R_a = 0.106 \mu\text{m}$, respectively.

C. Critical Heat Flux Model

The present experimental CHF and CHF values predicted by the model of Zuber [12], Lienhard and Dhir [13], Kandlikar [14], and Kim et al. [15] for $R_a = 0.106 \mu\text{m}$ are plotted in Fig. 8. The contact angle measured in the present study is used in Kandlikar’s and Kim’s models. The value of S and C is taken as 0.811 and 87.8, respectively, as suggested by Kim et al. [15]. The CHF value predicted by Zuber [12] and Lienhard and Dhir [13] is higher than the experimental CHF value. The effect of contact angle is considered by Kandlikar [14], whereas the effects of both surface roughness and contact angle are considered by Kim et al. [15] in their model. The capillary effect due to surface roughness is included in Kim’s model. The CHFs predicted by the models of Kandlikar [14] and Kim et al. [15] agree well with the present experimental CHF value at 1 bar. However, at high pressure, experimental values of CHF for $R_a = 0.106 \mu\text{m}$ are higher than the predicted values. Figure 9 shows the variation of experimental and predicted CHF by Kim’s model for the sample of R_a ranging from 0.106 to $4.03 \mu\text{m}$ at pressure up to 10 bar. It is found that the predicted values of CHF by Kim’s model are higher than the experimental CHF for the sample of higher surface roughness

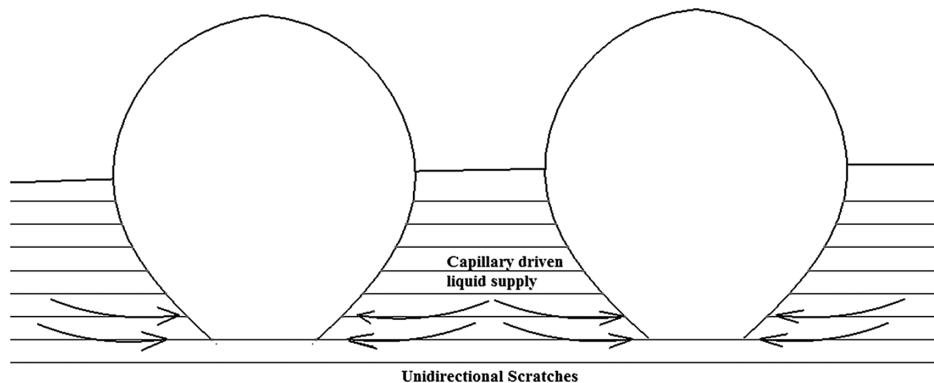


Fig. 6 Liquid supply through unidirectional scratches.

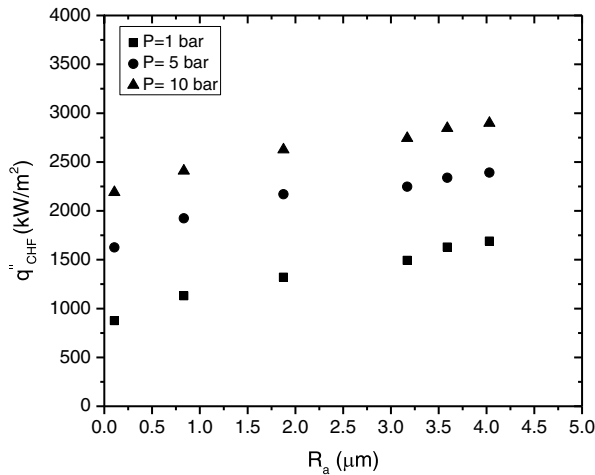


Fig. 7 Variation in CHF with R_a at different pressures.

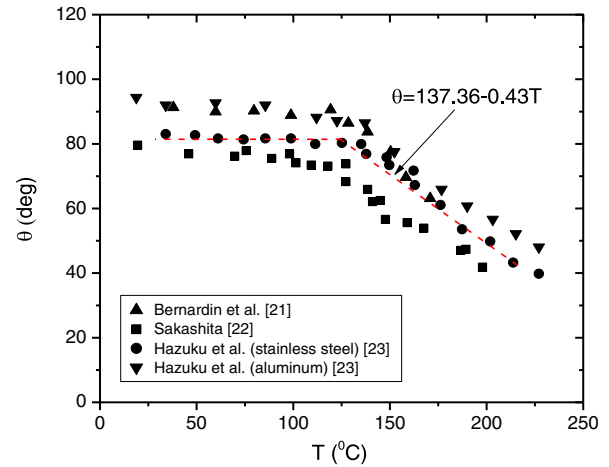


Fig. 10 Contact angle of water droplet at different temperatures.

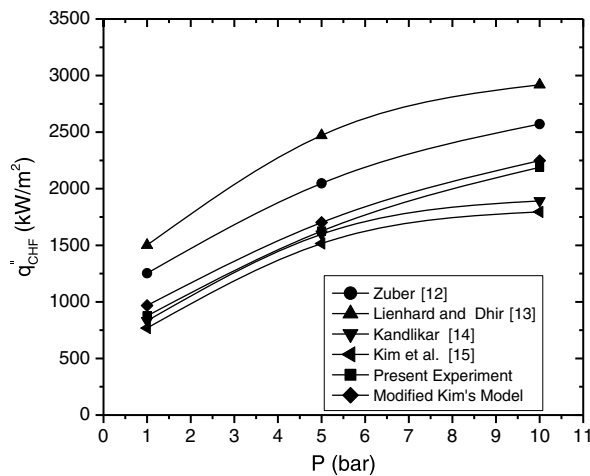


Fig. 8 Variation in CHF with pressure.

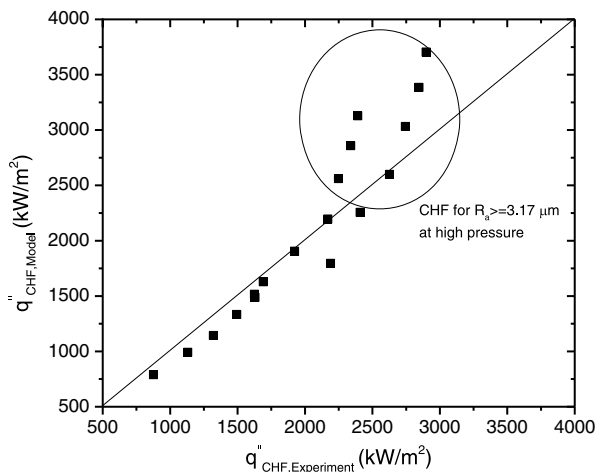


Fig. 9 Comparison of CHF predicted by the model of Kim et al. [15] with present experimental CHF.

($R_a \geq 3.17 \mu\text{m}$). This variation between experimental and predicted CHF values is obvious because the θ and C used for the CHF prediction at high pressure are measured at the atmospheric pressure. Kim et al. [15] conducted experiments at the atmospheric pressure and developed a CHF model that predicts their experimental values in

good agreement. To predict the CHF at high pressure, the parameters θ and C need to be determined at corresponding saturation temperature and system pressure. Bernardin et al. [21] studied the effect of temperature and pressure on the contact angle of water on a polished aluminum surface. They concluded that the contact angle is independent of pressure and is the function of saturation temperature. Recently, Sakashita [22] and Hazuku et al. [23] also reported the variation in the contact angle of the water droplet with the temperature. The contact angle of water on stainless steel and aluminum surfaces obtained in their study at different temperatures is shown in Fig. 10. The surface energy of copper and stainless steel is in the same range (1000–1100 mJ/m^2). Moreover the contact angle measured in the present study on the smooth surface of copper at the atmospheric temperature closely matches with the one measured on the smooth surface of stainless steel, reported by Hazuku et al. [23]. Hence, contact angle values reported by Hazuku et al. [23] at high temperatures are considered in the present study. They found that the contact angle decreases linearly with the gradient $d\theta/dT = -0.43$ beyond 120°C temperature, as shown in Fig. 10. The empirical relation is also developed between contact angle and surface roughness from the present contact angle measurement data, as shown in Fig. 3. Thus, considering both the relations given in Figs. 3 and 10, the combined effect of surface roughness and temperature on the contact angle ($\theta \propto R_a T_{\text{sat}}$) is estimated and incorporated in the Kim's model. In the present study, the value of C in the Kim's model is determined at different pressures by substituting measured data of θ , R_a , S_m , and experimental CHF value. Thus the value of C obtained for each sample at different pressure is tabulated in Table 5. Similar procedure was followed by Kim et al. [15] to estimate the value of C at the atmospheric pressure. As the proportionality constant C in the model implies the number of capillary tubes that lie underneath the bubble, the value of C found to be decreased with the increase in the pressure and with the increase in mean spacing between the scratches. Kim's model, given in Table 1, with modified S , C , and θ is used to predict the CHF. Thus predicted CHF is compared with present experimental data and presented in Fig. 11. The predicted CHF is found to be in good

Table 5 Value of C for each sample

R_a	$P = 1$ bar	$P = 5$ bar	$P = 10$ bar
0.106	70.90	65.25	64.12
0.83	34.31	26.91	25.83
1.87	28.54	21.50	20.52
3.17	26.17	18.45	18.20
3.59	25.84	18.15	18.08
4.03	25.33	18.06	17.90

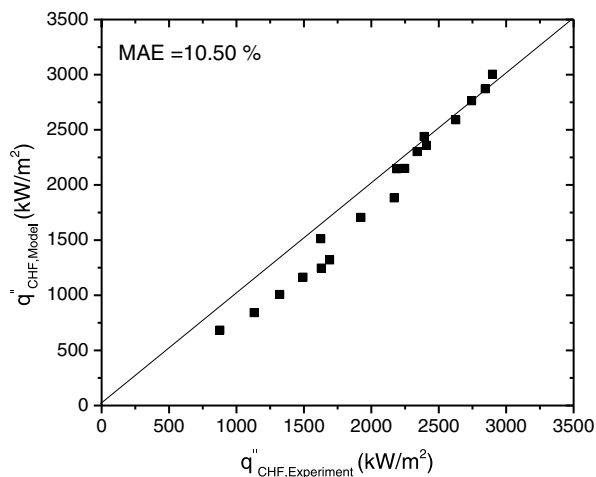


Fig. 11 Comparison of CHF predicted by modified Kim's model with present experimental CHF.

agreement with the experimental CHF with a mean absolute error (MAE), obtained by Eq. (5), of 10.50%.

$$MAE = \frac{1}{N} \sum \frac{|D_{b\text{pred}} - D_{b\text{exp}}|}{D_{b\text{exp}}} \times 100 \quad (5)$$

D. Bubble Departure Diameter

At each steady-state condition, the corresponding temperature and boiling video are recorded at 1, 5, and 10 bar system pressure for the samples of a wide range of R_a . The video is recorded up to the moment of bubble coalescence. Frames of isolated bubbles are selected from the recorded video to measure the instantaneous bubble diameter (d). Instantaneous bubble diameter is the diameter of the bubble measured during the bubble growth, that is, from its nucleation till the bubble departure. The variation in the instantaneous bubble diameter with the time period for all the samples at $P = 10$ bar is shown in Fig. 12. As evaporation takes place through the unidirectional scratches, bubble growth is inertia-controlled. Hence it is found that the instantaneous bubble diameter increases linearly with the time for all the samples. Ramaswamy et al. [24] also commented that during the inertia-controlled bubble growth, bubble grows linearly with the time period. The bubble departure diameter measured for the sample of different R_a is plotted as a function of Ja at different pressures as shown in Fig. 13. It illustrates that the bubble departure diameter increases linearly with the increase in Ja at all pressures. It is found that

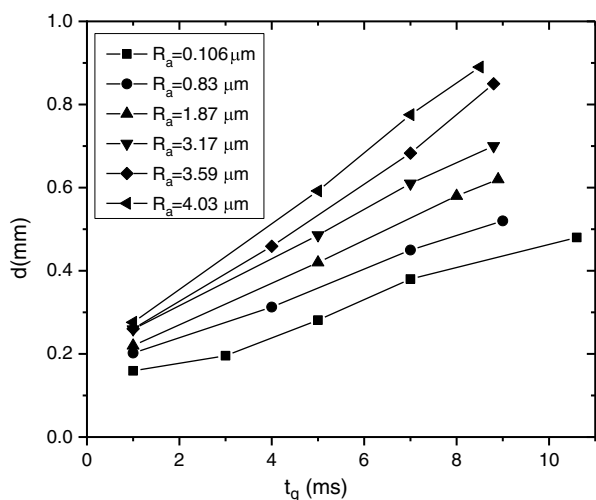


Fig. 12 Bubble growth curve for the sample of different R_a at $P = 10$ bar.

the wall superheat temperature is reduced with the increase in R_a . The bubble departure diameter is found to be increased with the increase in R_a at given Ja . In the present study, unidirectional scratches, which act as a liquid supply passage to the nucleated bubble, are made from different grits of SiC sandpaper. The spacing between two unidirectional scratches and R_a increased with the decrease in the grit of SiC sandpaper, which resulted in the higher cavity size of the nucleation site. This enlarges the bubble during its initial growth period. The combined effect of cavity size and unidirectional scratches resulted in the increase in the bubble departure diameter. It is also found that the bubble departure diameter decreases with the increase in the system pressure. The forces acting on the growing bubble need to be considered to justify this phenomenon. The bubble nucleated on the upward-facing surface experiences upward-acting forces, namely, buoyancy and lift force, whereas hydrostatic and surface tension forces act against the bubble growth. The surface tension force decreases with the increase in the temperature. The bubble detaches from the surface immediately after its initial growth phase. Hence the bubble departure diameter decreased with the increase in pressure, resulting in tiny bubbles departing from the surface.

The correlation for the bubble departure diameter available in the literature is in the form of $[\sigma/(g(\rho_l - \rho_v))]^{0.5}$. The measured bubble departure diameter is compared with that predicted by the correlation of Cole [16], Cole and Rohsenow [17], and Cole and Shulman [18]. The variation in the predicted bubble departure diameter with the experimental one for the smooth surface of $R_a = 0.106 \mu\text{m}$ at 1, 5, and 10 bar system pressure is shown in Fig. 14. The MAE and percentage deviation are considered for the statistical evaluation. MAEs between predicted and experimental bubble departure diameter are given in Table 6. The overall MAE of the predicted values by correlation of Cole [16] is below 20% for all experimental conditions considered in the present work. It is found in Fig. 14 that the correlation of Cole and Rohsenow [17] and Cole and Shulman [18] overpredicts the bubble departure diameter at $P = 1$ bar, whereas experimental values are higher than that of the predicted values at $P = 5$ bar and $P = 10$ bar. The bubble departure diameter predicted by Cole [16] is a function of Ja , whereas the correlation of Cole and Rohsenow [17] and Cole and Shulman [18] predicts the bubble departure diameter as a function of saturation temperature and pressure, respectively. As it is found in the present study that the bubble departure diameter is the function of Ja and pressure, the variation in the predicted and experimental values is considerably high.

E. Correlation for Bubble Departure Diameter

Forces in bubble dynamics classified as the unsteady growth force, buoyancy force, surface tension, lift force, and bubble inertia as discussed in [20] are considered to develop the form of correlation as given in Eq. (6). Bubble departs from the surface as upward-acting assisting forces on the bubble exceed the downward-acting forces. The bubble departure diameter is measured at the detachment of the bubble from the surface. Considering the force balance, the correlation for the bubble departure diameter is developed in the present work as described below.

$$F_{duy} + F_{st} + F_{bi} = F_{buy} + F_L \quad (6)$$

$$\begin{aligned} \frac{\pi}{6} D_b^3 g (\rho_l - \rho_v) + 2\pi \rho_l D_b^2 C_L \left(\frac{dr}{dt} \right)^2 &= 2\pi r_d \sigma \sin \theta \\ &+ \frac{3\pi}{8} C_s \rho_l D_b^2 \left(\frac{dr}{dt} \right)^2 + \frac{\pi}{8} \rho_l D_b^3 \frac{d^2 r}{dt^2} + \frac{\pi}{6} \rho_v D_b^3 \frac{d^2 r}{dt^2} + \pi \rho_v D_b^2 \left(\frac{dr}{dt} \right)^2 \end{aligned} \quad (7)$$

Rearranging the above terms,

$$\begin{aligned} \frac{\pi}{6} D_b^3 g (\rho_l - \rho_v) &= 2\pi r_d \sigma \sin \theta + \left[\frac{3C_s \rho_l}{8} - 2C_L \rho_l + \rho_v \right] \pi D_b^2 \left(\frac{dr}{dt} \right)^2 \\ &+ \frac{\pi}{2} \left[\frac{\rho_l}{4} + \frac{\rho_v}{3} \right] D_b^3 \frac{d^2 r}{dt^2} \end{aligned} \quad (8)$$

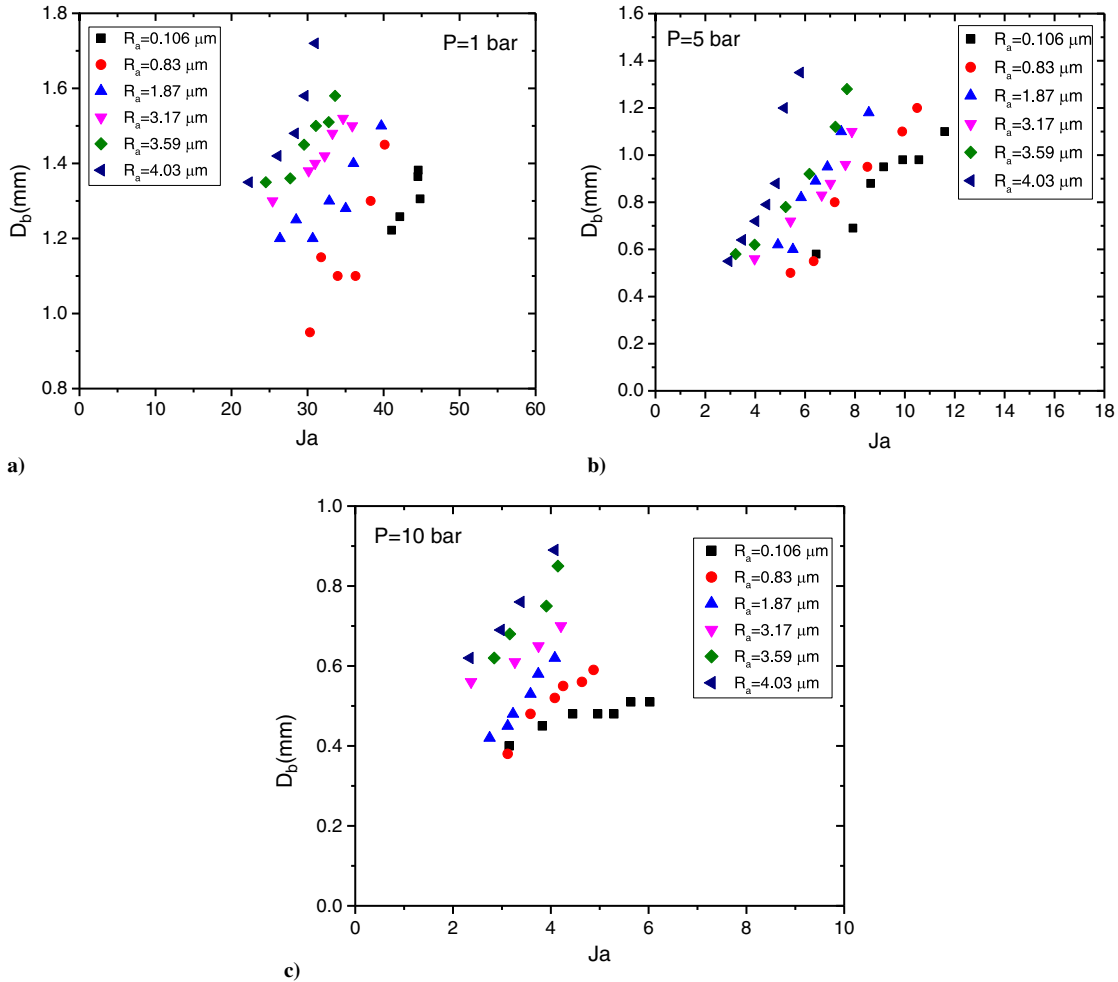


Fig. 13 Variation in the bubble departure diameter with Ja at a) $P = 1$ bar, b) $P = 5$ bar, and c) $P = 10$ bar.

As $\rho_l \gg \rho_v$ the summation of ρ_l and ρ_v is approximated to ρ_l .

$$\frac{\pi}{6} D_b^3 g(\rho_l - \rho_v) = 2\pi r_d \sigma \sin \theta + \left[\frac{3C_s}{8} - 2C_L \right] \pi \rho_l D_b^2 \left(\frac{dr}{dt} \right)^2 + \frac{\pi}{8} \rho_l D_b^3 \frac{d^2 r}{dt^2} \quad (9)$$

Dividing Eq. (9) by $\pi \sigma D_b / 6$

$$\frac{D_b^2 g(\rho_l - \rho_v)}{\sigma} = \frac{12r_d \sin \theta}{D_b} + \left[\frac{3C_s}{8} - 2C_L \right] \frac{6\rho_l D_b}{\sigma} \left(\frac{dr}{dt} \right)^2 + \frac{3\rho_l D_b^2}{4\sigma} \left(\frac{d^2 r}{dt^2} \right) \quad (10)$$

The bubble growth can be formulated from the heat balance between conduction heat transfer through the microlayer and latent heat transfer by the bubble. It is observed in Fig. 12 that bubble growth is a linear function of time. Hence the bubble growth rate can be expressed as given in Eq. (11).

$$\frac{dr}{dt} = C_t \frac{k\Delta T}{R\rho_v h_{fg}} \quad (11)$$

$$\frac{d^2 r}{dt^2} = \left(\frac{-2}{D_b} \right) \left(\frac{dr}{dt} \right)^2 \quad (12)$$

Equation (13) is derived from Eqs. (10)–(12).

$$\frac{D_b^2 g(\rho_l - \rho_v)}{\sigma} = \frac{12r_d \sin \theta}{D_b} + \left[\frac{3C_s}{8} - 2C_L \right] \left(\frac{6\rho_l D_b}{\sigma} \right) \frac{C_t^2 k^2 \Delta T^2}{R^2 \rho_v^2 h_{fg}^2} + \frac{3\rho_l D_b^2}{4\sigma} \left(\frac{-2}{D_b} \right) \frac{C_t^2 k^2 \Delta T^2}{R^2 \rho_v^2 h_{fg}^2} \quad (13)$$

$$B_o^{3/2} = \frac{12r_d \sin \theta}{D_b} \left(B_o^{1/2} \right) + [9C_s C_t^2 - 48C_L C_t^2 - 6C_t^2] K_l \quad (14)$$

where $B_o = D_b^2 g(\rho_l - \rho_v) / \sigma$, $K_l = (Ja / Pr_l)^2 Ar^{-1}$, $Ar = [g\rho_l(\rho_l - \rho_v) / \mu_l^2][\sigma / g(\rho_l - \rho_v)]^{3/2}$.

The dry-out radius of the bubble at departure is very small compared with the bubble departure diameter; hence, the value of r_d / D_b will be close to zero, and thus the first term in Eq. (14) is neglected. The proportional relation of B_o with K_l is expressed in Eq. (15).

$$B_o^{3/2} \sim [9C_s C_t^2 - 48C_L C_t^2 - 6C_t^2] K_l \quad (15)$$

To fit the experimental data, the linear dependence can be written as given in Eq. (16).

$$B_o^{1/2} = (\omega_1 + \omega_2 K_l)^{1/3} \quad (16)$$

Based on the experimental data, the fitting parameters ω_1 and ω_2 are obtained. The relationship between B_o and K_l is presented in Eq. (17).

$$B_o^{1/2} = (0.02 + 1018.5)^{1/3} \quad (17)$$

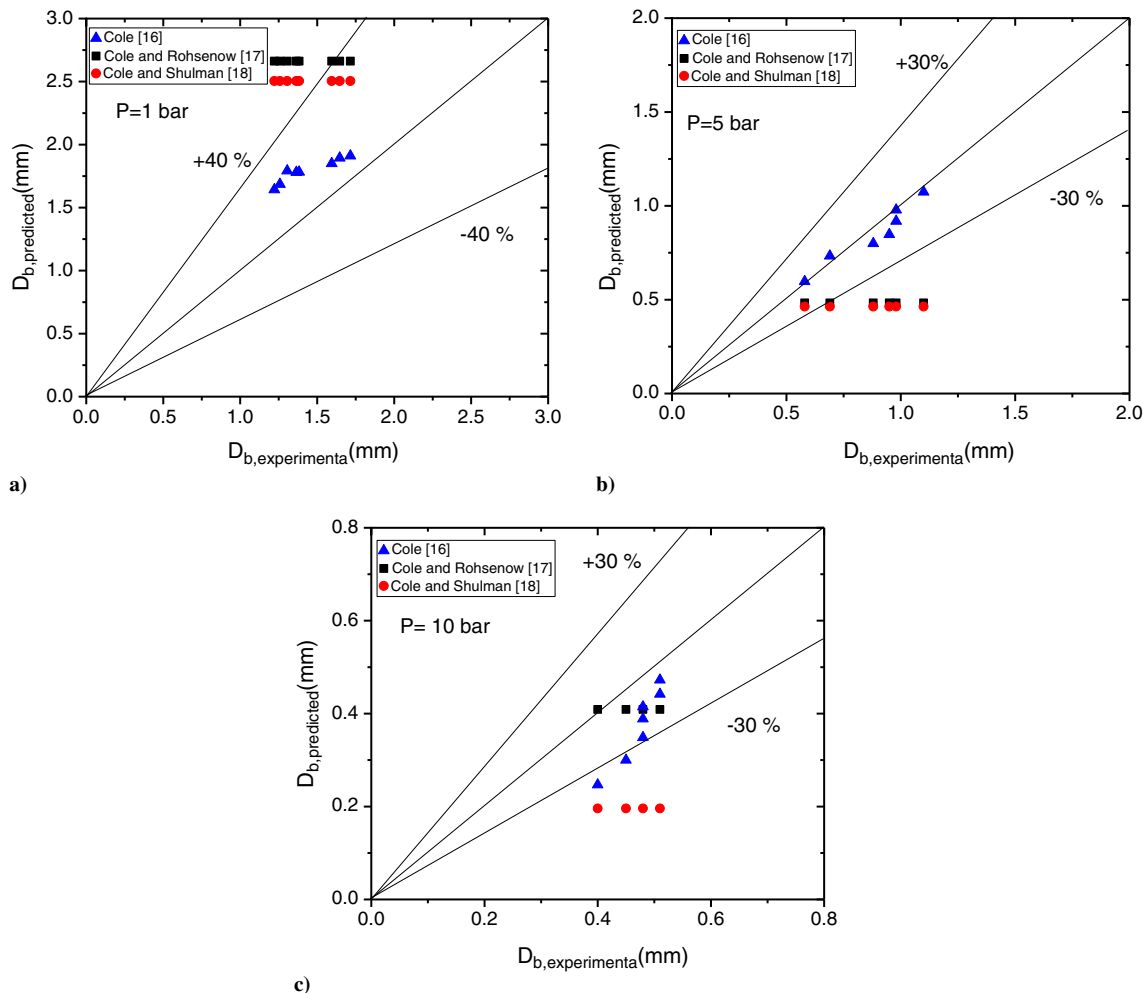


Fig. 14 Variation in the predicted bubble departure diameter with the corresponding experimental values at a) $P = 1$ bar, b) $P = 5$ bar, and c) $P = 10$ bar.

The final expression of the present correlation for the bubble departure diameter of the sample of R_a ranging from 0.106 to 4.03 μm at 1, 5, and 10 bar system pressure is given in Eq. (18).

$$D_b = (0.02 + 1018.5K_I)^{1/3} \left[\frac{\sigma}{g(\rho_l - \rho_v)} \right]^{1/2} \quad (18)$$

Similar form of correlation is derived by Chen et al. [19] for the prediction of the bubble departure diameter of methane. Figure 15 shows the comparison between the predicted and experimental values of the bubble departure diameter. The predicted bubble departure diameter is within $\pm 30\%$ deviation. The MAE between predicted and experimental values of the bubble diameter is 17.83%. It illustrates that the values predicted by the present correlation are in good agreement with the experimental values.

F. Bubble Frequency

Bubble frequency is the reciprocal of sum of waiting period and growth period of the bubble. Bubble frequency is estimated by 30 consecutive bubbles. The bubble frequency for the sample of

different R_a is plotted as a function of Ja at different pressures in Fig. 16. It is observed that the bubble frequency increases with the increase in Ja . It is also observed that the bubble frequency increases with the increase in R_a at constant Ja at all the pressures. The bubble growth is classified into two phases: initial growth stage and final growth stage. The initial stage is dominated by the heat transfer, whereas the kinetic effect plays a significant role during the final stage of the bubble growth. The enhanced heat transfer due to the increase in R_a stimulates the initial stage of bubble growth wherein hemispherical bubble grows over the nucleation cavity. Thus the bubble growth period substantially dropped with the increase in heat flux and Ja . The bubble dynamics plays a vital role in the final stage of bubble growth. Buoyancy force becomes dominant as the bubble grows larger in diameter in its initial stage of growth. This leads to the early bubble departure. Thus the overall growth period decreases with the increase in Ja . The unidirectional scratches offer intense liquid supply through capillary action. The liquid rushes toward the bubble base, which causes the vapor to get entrapped at the bubble neck. Thus the waiting period between two consecutive bubble nucleations decreased with the increase in wall superheat. At high heat flux, the waiting period is found to be negligible. The combined reduction in growth period and waiting period resulted in the increase in bubble frequency.

The correlations used in the present study to compare the experimental data are in the form of fD_b^n . The values of $fD_b^{1/2}$ and fD_b at different pressures are obtained from the experimental data for $R_a = 0.106 \mu\text{m}$ and compared with the value predicted from correlations of Cole [25], Zuber [26], and Jakob and Fritz [27] as shown in Figs. 17a, 17b, and 17c, respectively. At 5 and 10 bar pressure, the correlation of Cole [25] predicted the experimental

Table 6 MAE between predicted and measured bubble departure diameter

Correlation	$P = 1$ bar	$P = 5$ bar	$P = 10$ bar
Cole [16]	25.95%	5.42%	21.75%
Cole and Rohsenow [17]	88.09%	42.66%	13.64%
Cole and Shulman [18]	76.96%	44.97%	58.29%

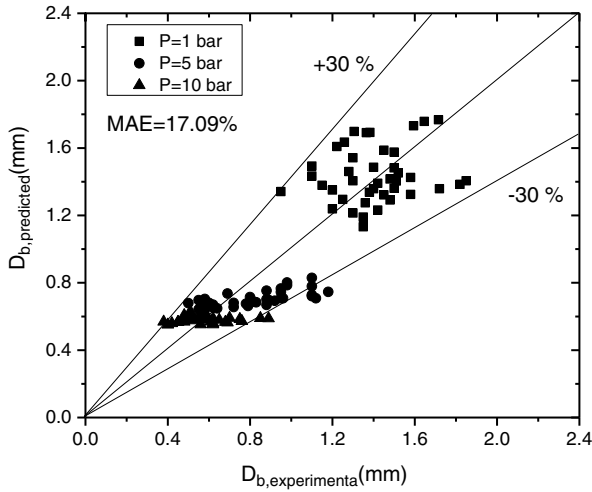


Fig. 15 Comparison between predicted bubble departure diameter from present correlation and present experimental value.

value of $fD_b^{1/2}$ within $\pm 40\%$ deviation with the MAE of 28.71%, whereas it predicts the experimental value at 1 bar beyond $+40\%$ deviation. The correlation of Zuber [26] is based on the thermophysical properties of the liquid, and thus the predicted fD_b varies with pressure, as shown in Fig. 17b. It predicts the experimental fD_b within $\pm 40\%$ deviation for 1 and 5 bar pressure, whereas the predicted fD_b found to be beyond $+40\%$ deviation from the experimental values at 10 bar. The correlation of Jakob and Fritz [27] predicts the experimental fD_b similar to that of Zuber [26].

The correlations considered in the present study cannot predict the experimental data at different R_a . In this study, pool boiling of water with the sample of different R_a at pressure up to 10 bar is carried. The correlation is developed in the form of fD_b^2 by fitting the experimental data of the present study. The form of correlation is developed by considering the bubble waiting period, bubble growth period, and bubble growth rate. Bubble frequency (f), as given in Eq. (19), is the reciprocal of sum of growth period and waiting period of the bubble.

$$f = \frac{1}{t_g + t_w} \quad (19)$$

Bubble growth rate as suggested by Chen et al. [19] can be expressed as given in Eq. (20).

$$\frac{dr}{dt} = \frac{C_t k \Delta T}{R \rho_v h_{fg}} = \frac{C_t J a \alpha_l}{R} \quad (20)$$

where C_t is proportionality constant.

Bubble growth period (t_g) is the transient bubble growth from its nucleation till the departure. R is the bubble radius at its departure. Integrating Eq. (21)

$$\int_0^R R dr = C_t J a \alpha_l \int_0^{t_g} dt \quad (21)$$

$$t_g = \frac{R^2}{2C_t J a \alpha_l} \quad (22)$$

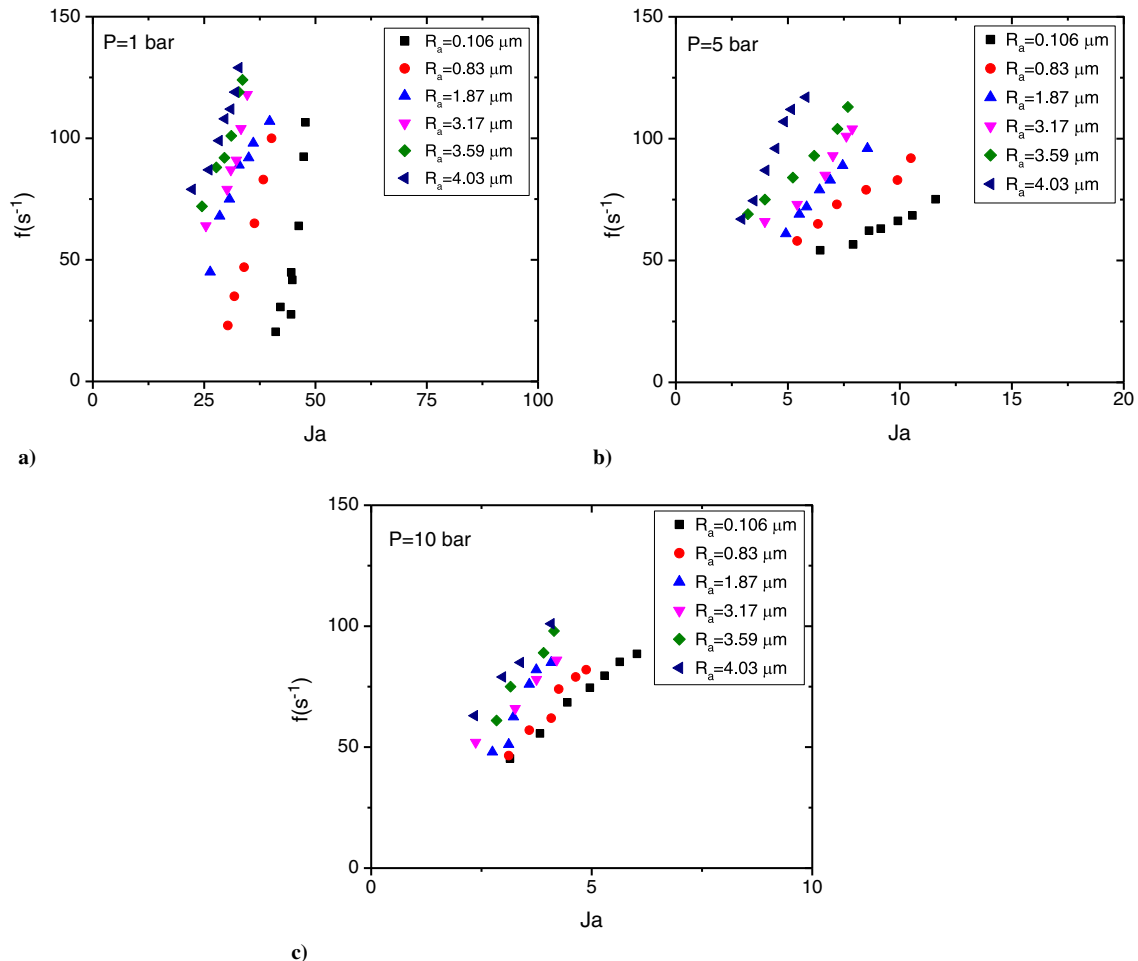


Fig. 16 Variation in bubble frequency with Ja at a) $P = 1$ bar, b) $P = 5$ bar, and c) $P = 10$ bar.

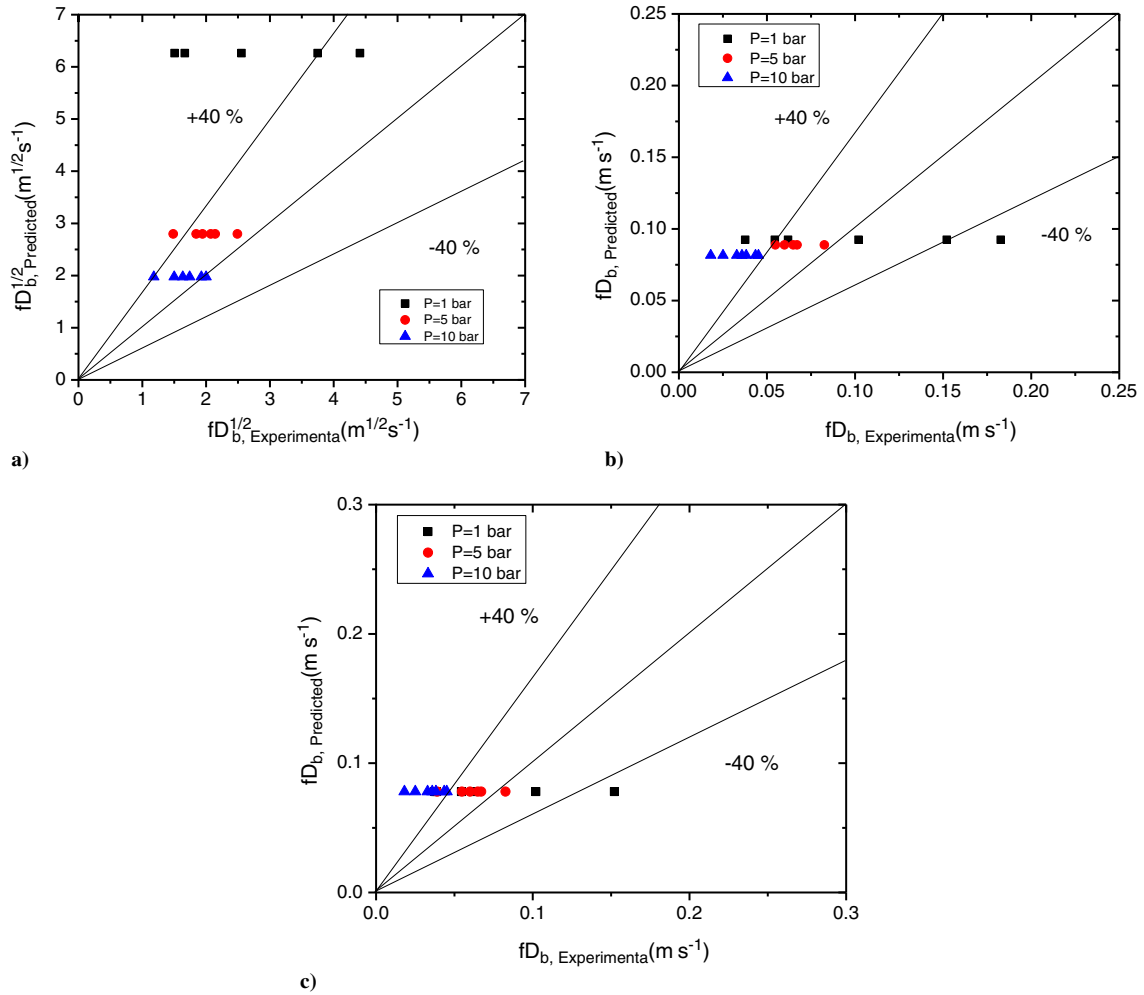


Fig. 17 Comparison of predicted fD_b^2 by a) Cole [25], b) Zuber [26], and c) Jakob and Fritz [27] with the corresponding experimental value.

The waiting period (t_w) is defined as the time interval from the detachment of a preceding bubble to the nucleation of a following bubble. Liquid replenishment toward the nucleation site takes place immediately after the bubble departure. Thermal layer develops over the nucleation site during the waiting period of the bubble cycle. The thickness of thermal layer developed during this period is given by Cooper [28] and is expressed in Eq. (23).

$$\delta = (\pi \alpha_l t_w)^{1/2} \quad (23)$$

$$t_w = \frac{\delta^2}{\pi \alpha_l} \quad (24)$$

Kutateladze and Gogonin [29] suggested that the radius of the bubble is proportional to the thermal layer developed. Thus considering $\delta = xR$, Eq. (24) becomes

$$t_w = \frac{x^2 R^2}{\pi \alpha_l} \quad (25)$$

Combining Eqs. (19), (22), and (25), bubble frequency is expressed as given in Eq. (26).

$$f = \frac{8\pi C_l Ja \alpha_l}{D_b^2 (\pi + 2x^2 C_l Ja)} \quad (26)$$

The form of the correlation is expressed in terms of fD_b^2 in Eq. (27), where ω_3 and ω_4 are the fitting parameters.

$$\frac{fD_b^2}{Ja \alpha_l} = \frac{8\pi C_l}{(\pi + 2x^2 C_l Ja)} = \frac{\omega_3}{\pi + \omega_4 Ja} \quad (27)$$

Considering experimental data, the fitting parameters are obtained. Thus the correlation for the relation between bubble departure diameter and bubble frequency is developed as given in Eq. (28).

$$fD_b^2 = \left(\frac{43.07}{1 + 3.18 \times 10^{-4} Ja} \right) Ja \alpha_l \quad (28)$$

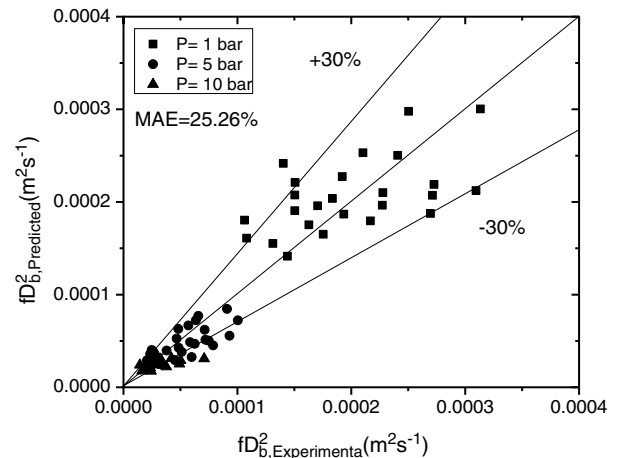


Fig. 18 Comparison of present correlation for fD_b^2 with the experimental value.

Figure 18 shows the variation in the predicted fD_b^2 with experimental values at pressure of 1, 5, and 10 bar. The deviation between predicted and experimental fD_b^2 is found within ± 30 for all the pressures. The correlation developed in the present study can predict the experimental value with MAE of 25.26%. Thus it is commented that the present correlation is in good agreement with the experimental values in the investigated range of R_a varying from 0.106 to 4.03 μm at pressures up to 10 bar.

IV. Conclusions

Investigation of pool boiling heat transfer was conducted with samples of R_a ranging from 0.106 to 4.03 μm at pressures 1, 5, and 10 bar. Desired surface roughness was achieved by the formation of unidirectional scratches using different grit SiC sandpapers. The effect of R_a on CHF was studied. The effect of R_a on the bubble departure diameter and bubble frequency was reported at different pressures. CHF was predicted by incorporating the temperature and roughness effects on the contact angle. The correlation for the bubble departure diameter and fD_b^2 was developed considering the present bubble dynamics study. Following comments are drawn based on the present investigation:

1) CHF increased with the increase in R_a as well as pressure. The CHF of $R_a = 4.03 \mu\text{m}$ at 1, 5, and 10 bar was found to be 92.85, 47.11, and 32.38% higher than that of $R_a = 0.106 \mu\text{m}$, respectively.

2) The effect of temperature and R_a on the contact angle was considered in the modified CHF model, which predicts the present CHF values with MAE of 10.50%.

3) Bubble departure diameter and bubble frequency increased with the increase in Ja as well as R_a for investigated range of parameters. The increased cavity size and enhanced capillary-induced liquid supply due to unidirectional scratches played an important role in bubble dynamics.

4) The correlation developed for bubble departure diameter was found to be in good agreement with the measured bubble departure diameter where it predicts the experimental values with MAE of 17.83%.

5) The deviation between predicted and experimental fD_b^2 was found to be within ± 30 , whereas MAE was found to be 25.26%.

References

- [1] Bland, T. J., Downing, R. S., and Rogers, D. P., "A Two-Phase Thermal Management System for Large Space Platforms," AIAA Paper 1984-1578, June 1984. doi:10.2514/6.1984-1758
- [2] Ellis, W. E., "The Space Station Active Thermal Control Technical Challenge," AIAA Paper 1989-0073, Jan. 1989. doi:10.2514/6.1989-73
- [3] Qiu, D. M., Dhir, V. K., Chao, D., Hasan, M. M., Neumann, E., Yee, G., and Birchenough, A., "Single-Bubble Dynamics During Pool Boiling Under Low Gravity Conditions," *Journal of Thermophysics and Heat Transfer*, Vol. 16, No. 3, 2002, pp. 336–345. doi:10.2514/2.6710
- [4] Jones, B. J., McHale, J. P., and Garimella, S. V., "The Influence of Surface Roughness on Nucleate Pool Boiling Heat Transfer," *Journal of Heat Transfer*, Vol. 131, No. 12, 2009, Paper 121009. doi:10.1115/1.3220144
- [5] Phan, H., Caney, N., Marty, P., and Colasson, J., "Surface Wettability Control by Nanocoating: The Effects on Pool Boiling Heat Transfer and Nucleation Mechanism," *International Journal of Heat and Mass Transfer*, Vol. 52, Nos. 23–24, 2009, pp. 5459–5471. doi:10.1016/j.ijheatmasstransfer.2009.06.032
- [6] Kim, B. H., and Peterson, G. P., "Effect of Morphology of Carbon Nanotubes on Thermal Conductivity Enhancement of Nanofluids," *Journal of Thermophysics and Heat Transfer*, Vol. 21, No. 3, 2007, pp. 451–459. doi:10.2514/1.18341
- [7] Shukla, K. N., Brusly Solomon, A., Pillai, B. C., and Ibrahim, M., "Thermal Performance of Cylindrical Heat Pipe Using Nanofluids," *Journal of Thermophysics and Heat Transfer*, Vol. 24, No. 4, 2010, pp. 796–802. doi:10.2514/1.48749
- [8] Mohamadifard, K., Zeinali, H., and Saeed, H. M., "Experimental Investigation of Pool Boiling Performance of Alumina/Ethylene-Glycol/Water (60/40) Nanofluids," *Journal of Thermophysics and Heat Transfer*, Vol. 28, No. 4, 2014, pp. 724–734. doi:10.2514/1.14071
- [9] Li, C. H., "Nucleate Boiling Heat Transfer on Sintered Copper Porous Structure Module Cone Surfaces," *Journal of Thermophysics and Heat Transfer*, Vol. 25, No. 1, 2011, pp. 186–192. doi:10.2514/1.49106
- [10] Chao, D. F., Zhang, N., and Yang, W.-J., "Nucleate Pool Boiling on Copper-Graphite Composite Surfaces and its Enhancement Mechanism," *Journal of Thermophysics and Heat Transfer*, Vol. 18, No. 2, 2004, pp. 236–242. doi:10.2514/1.1103
- [11] Kutateladze, S. S., "A Hydrodynamic Theory of Changes in a Boiling Process Under Free Convection," *Izvestia Akademia Nauk, S.S.S.R., Otdelenie Tekhnicheskii Nauk*, Vol. 4, Jan. 1951, pp. 529–536.
- [12] Zuber, N., "Hydrodynamic Aspects of Boiling Heat Transfer," Univ. of California, 4439, Los Angeles, June 1959. doi:10.2172/4175511
- [13] Lienhard, J. H., and Dhir, V. K., "Extended Hydrodynamic Theory of the Peak and Minimum Pool Boiling Heat Fluxes," NASA CR-2270, July 1973.
- [14] Kandlikar, S. G., "A Theoretical Model to Predict Pool Boiling CHF Incorporating Effects of Contact Angle and Orientation," *Journal of Heat Transfer*, Vol. 123, No. 6, 2001, pp. 1071–1079. doi:10.1115/1.1409265
- [15] Kim, J., Jun, S., Laksnarain, R., and You, S. M., "Effect of Surface Roughness on Pool Boiling Heat Transfer at a Heated Surface Having Moderate Wettability," *International Journal of Heat and Mass Transfer*, Vol. 101, Oct. 2016, pp. 992–1002. doi:10.1016/j.ijheatmasstransfer.2016.05.067
- [16] Cole, R., "Bubble Frequencies and Departure Volumes at Subatmospheric Pressures," *AICHE Journal*, Vol. 13, No. 4, 1967, pp. 779–783. doi:10.1002/(ISSN)1547-5905
- [17] Cole, R., and Rohsenow, W. M., "Correlation of Bubble Departure Diameters for Boiling of Saturated Liquids," *Chemical Engineering Progress Symposium Series*, Vol. 65, No. 92, 1969, pp. 211–213.
- [18] Cole, R., and Shulman, H. L., "Bubble Departure Diameters at Subatmospheric Pressures," *Chemical Engineering Progress Symposium Series*, Vol. 62, No. 64, 1966, pp. 6–16.
- [19] Chen, H., Chen, G., Zou, X., Yao, Y., and Gong, M., "Experimental Investigations on Bubble Departure Diameter and Frequency of Methane Saturated Nucleate Pool Boiling at Four Different Pressures," *International Journal of Heat and Mass Transfer*, Vol. 112, Sept. 2017, pp. 662–675. doi:10.1016/j.ijheatmasstransfer.2017.05.031
- [20] Walunj, A., and Sathyabhama, A., "Comparative Study of Pool Boiling Heat Transfer from Various Microchannel Geometries," *Applied Thermal Engineering*, Vol. 128, Jan. 2018, pp. 672–683. doi:10.1016/j.applthermaleng.2017.08.157
- [21] Bernardin, J. D., Mudawar, I., Walsh, C. B., and Frances, E. I., "Contact Angle Temperature Dependence for Water Droplets on Practical Aluminum Surfaces," *International Journal of Heat and Mass Transfer*, Vol. 40, No. 5, 1997, pp. 1017–1033. doi:10.1016/0017-9310(96)00184-6
- [22] Sakashita, H., "Critical Heat Flux on a Vertical Surface in Saturated Pool Boiling at High Pressures," *Journal of Thermal Science and Technology*, Vol. 11, No. 2, 2016, Paper JTST0020. doi:10.1299/jtst.2016jtst0020
- [23] Hazuku, T., Fukuhara, Y., Takamasa, T., Hirose, Y., Hayashi, T., and Pollman, A. G., "Effect of Radiation on Surface Wettability Under High-Temperature and High-Pressure Environment," *Transactions of Japan Society of Mechanical Engineers Series B*, Vol. 75, No. 758, 2009, pp. 1911–1916. doi:10.1299/kikaib.75.758_1911
- [24] Ramaswamy, C., Joshi, Y., Nakayama, W., and Johnson, W. B., "High-Speed Visualization of Boiling from an Enhanced Structure," *International Journal of Heat and Mass Transfer*, Vol. 45, No. 24, 2002, pp. 4761–4771. doi:10.1016/S0017-9310(02)00196-5
- [25] Cole, R., "A Photographic Study of Pool Boiling in the Region of the Critical Heat Flux," *AICHE Journal*, Vol. 6, No. 4, 1960, pp. 533–538. doi:10.1002/(ISSN)1547-5905

- [26] Zuber, N., "Nucleate Boiling. The Region of Isolated Bubbles and the Similarity with Natural Convection," *International Journal of Heat and Mass Transfer*, Vol. 6, No. 1, 1963, pp. 53–78.
doi:10.1016/0017-9310(63)90029-2
- [27] Jakob, M., and Fritz, W., "Versuche über den Verdampfungsvorgang," *Forschung im Ingenieurwesen*, Vol. 2, No. 12, 1931, pp. 435–447.
doi:10.1007/BF02578808
- [28] Cooper, M. G., and Lloyd, A. J. P., "The Microlayer in Nucleate Pool Boiling," *International Journal of Heat and Mass Transfer*, Vol. 12, No. 8, 1969, pp. 895–913.
doi:10.1016/0017-9310(69)90154-9
- [29] Kutateladze, S. S., and Gogonin, I. I., "Growth Rate and Detachment Diameter of a Vapor Bubble in Free Convection Boiling of a Saturated Liquid," *Teplofizika Vysokikh Temperatur*, Vol. 17, Dec. 1979, pp. 792–797.